Mössbauer-Effect and Fenske–Hall Molecular Orbital Study of the Electronic Properties of a Series of Organoiron Butterfly Clusters

Margaret L. Buhl and Gary J. Long*

Department of Chemistry, University of Missouri—Rolla, Rolla, Missouri 65401-0249

James F. O'Brien

Department of Chemistry, Southwest Missouri State University, Springfield, Missouri 65804-0089

Received November 30, 1992

The electronic properties of a series of organoiron butterfly clusters, $HFe_4(CO)_{12}(\eta^2\text{-}CH)$ (I), $(PPN)[HFe_4(CO)_{12}C]$ (II), $(BzNMe_3)_2[Fe_4(CO)_{12}C]$ (III), $(PPN)[RhFe_3(CO)_{12}C]$ (IV), $Fe_4(CO)_{13}C$ (V), $(PPN)[MnFe_3(CO)_{13}C]$ (VI), $(PPN)_2[CrFe_3(CO)_{13}C]$ (VII), $(PPN)_2[WFe_3(CO)_{13}C]$ (VIII), $(PPN)[CrFe_3(CO)_{13}(CH)]$ (IX), $(PPN)[WFe_3(CO)_{13}(CH)]$ (X), $HCrFe_3(CO)_{13}(CH)$ (XI), and $HWFe_3(CO)_{13}(CH)$ (XII), have been studied both experimentally by the Mössbauer effect at 78 K and theoretically with Fenske–Hall molecular orbital calculations. In these clusters the Mössbauer-effect isomer shifts range from −0.225 to −0.029 mm/s for the unprotonated wingtip iron sites, from −0.018 to 0.141 mm/s for the backbone iron sites, and from 0.009 to 0.124 mm/s for the protonated wingtip iron sites. The quadrupole splittings range from 1.026 to 1.829 mm/s for the unprotonated wingtip iron sites, from 0.469 to 1.659 mm/s for the backbone iron sites, and from 0.831 to 1.183 mm/s for the protonated wingtip iron sites. The larger observed quadrupole splittings of the wingtip iron atoms indicate that their electronic environment is more distorted than that of the backbone iron atoms. In the anionic clusters the anionic charge is found to be delocalized predominately onto the oxygen of the carbonyl ligands. The carbide and carbonyl ligands become more negative as the electronegativity of the cluster heterometal decreases. As the carbide and carbonyl ligands donate electron density to the metal, the iron electronic configuration, which begins at $4s^03d^84p^0$, becomes on average $4s^{0.37}3d^{6.74}4p^{0.85}$, with a range from $4s^{0.34}3d^{6.76}4p^{0.72}$ in I to $4s^{0.38}3d^{6.71}4p^{0.93}$ in VI. The isomer shifts of the backbone and protonated wingtip iron sites are more positive than those of the unprotonated wingtip iron site because, for the former, the iron 4s to ligand overlap population is less than for the latter. The iron 4s-electron density, as measured experimentally at the iron-57 nucleus by the Mössbauer-effect isomer shift, decreases as expected with an increase in the sum of the iron 4s Mulliken atomic orbital population and the Clementi and Raimondi effective nuclear charge. The isomer shift is also found to decrease as the iron 4s to near-neighbor overlap population increases. The calculated quadrupole splittings, obtained from the Fenske–Hall molecular orbital wave functions, agree rather well with the observed quadrupole splittings.

Introduction

The importance of iron butterfly clusters as catalysts, catalytic precursors, and models of metal surfaces during the processes of chemisorption and catalysis has been presented elsewhere.[1] The structural and electronic properties of several organoiron butterfly clusters have been successfully studied by using the results of Fenske–Hall molecular orbital calculations.[2-6] For instance, in the butterfly cluster $HFe_4(CO)_{12}(\eta^2\text{-}CH)$ (I) the preference of the bridged orientation of the CH ligand over the unbridged orientation may be explained in terms of the interaction of an unoccupied $[CH]^-$ fragment orbital with an occupied $[HFe_4(CO)_{12}]^+$ fragment orbital. The bridging-ligand orientation is stabilized because the carbon atom is bound more strongly to "the iron atoms of one of the butterfly's triangular wings",[2] and simultaneously, the hydrogen atom is bound to the other wingtip iron atom. In a study[3] of the bonding in $[Fe_4(CO)_{12}C]^{2-}$ (III), the bonding within the $[Fe_4(CO)_{12}]^{2+}$ fragment was first investigated, and subsequently $[Fe_4(CO)_{12}]^{2+}$ was combined with a $[C]^{4-}$ fragment. The $[Fe_4(CO)_{12}]^{2+}$ fragment reveals that the major iron–iron bonding occurs in the occupied molecular orbitals of high energy which contain iron 4s, 3d, and 4p atomic orbital character. The low-energy unoccupied $[Fe_4(CO)_{12}]^{2+}$ fragment orbitals interact with the occupied carbon 2p atomic orbitals in the $[C]^{4-}$ fragment to form the iron–carbon bonds in the final clusters. The molecular orbitals of $[Fe_4(CO)_{12}C]^{2-}$ involved in the iron–iron bonding are themselves different in that some are localized along the edges of the butterfly framework between the wingtip and the backbone iron atoms, others are localized between the two backbone iron atoms, and still others are delocalized across the faces of the butterfly framework. The frontier orbitals of $[Fe_4(CO)_{12}C]^{2-}$ (III) are predominately iron in character,

(1) Buhl, M. L. Ph.D. Thesis, University of Missouri—Rolla, 1993.
(2) Housecroft, C. E.; Fehlner, T. P. *Organometallics* **1983**, *2*, 690–692.
(3) Harris, S.; Bradley, J. S. *Organometallics* **1984**, *3*, 1086–1093.
(4) Wang, J.; Crespi, A. M.; Sabat, M.; Harris, S.; Woodcock, C.; Shriver, D. F. *Inorg. Chem.* **1989**, *28*, 697–703.
(5) Harris, S.; Blohm, M. L.; Gladfelter, W. L. *Inorg. Chem.* **1989**, *28*, 2290–2297.
(6) Bradley, J. S.; Harris, S.; Newsam, J. M.; Hill, E. W.; Leta, S.; Modrick, M. A. *Organometallics* **1987**, *6*, 2060–2069.

0276-7333/93/2312-1902$04.00/0

and thus, when $[Fe_4(CO)_{12}C]^{2-}$ (III) is either protonated to form $[HFe_4(CO)_{12}C]^-$ (II) or reacted with carbon monoxide to form $Fe_4(CO)_{13}C$ (V), the proton or the carbonyl ligand adds to the iron framework of the parent cluster rather than to the carbide.[3]

Heterometallic butterfly clusters permit the study[7-12] of the influence of another transition metal on the structure, reactivity, and electronic properties of the cluster. Hriljac et al.[11] found that, in a heterometallic butterfly cluster in which the heterometal occupies a backbone position, initial protonation occurs across a wingtip iron to carbide bond, rather than across the backbone as occurs upon protonation of $[Fe_4(CO)_{12}C]^{2-}$.[7,11,13] The differences in the character of the higher occupied frontier orbitals in the heterometallic clusters and $[Fe_4(CO)_{12}C]^{2-}$ may be used to explain[7] the difference in the preferred protonation site. For instance, the higher occupied frontier orbitals of $[RhFe_3(CO)_{12}C]^-$ do not contain any backbone rhodium atomic orbital character but do contain some carbide atomic orbital character. This, coupled with the absence of a frontier molecular orbital solely localized across the backbone of the butterfly framework, leads to protonation across a wingtip iron–carbon bond to form $RhFe_3(CO)_{12}(CH)$. The higher occupied frontier orbitals in $[MnFe_3(CO)_{13}C]^-$ contain both wingtip iron and backbone manganese atomic orbital character. It has also been found[7] in $[MnFe_3(CO)_{13}C]^-$ that the frontier orbitals containing backbone iron and manganese atomic orbital character are used for bonding by the bridging carbonyl and are therefore unavailable for protonation. As a result, protonation occurs across a wingtip iron–carbon bond.

The differences in the electronic properties of heterometallic and homometallic butterfly clusters are also influenced by differences in the energy of the metal *n*d orbitals and changes in point group symmetry from C_{2v} to C_s.[7,13] The orbital energy is related to the nuclear charge of an atom. As this charge increases, the orbital energy decreases because of the increased attraction between the nucleus and the electrons.[14] The HOMO of $[RhFe_3(CO)_{12}C]^-$ does not contain any rhodium atomic orbital character[7] because the rhodium 4d atomic orbitals are somewhat lower in energy than the iron 3d atomic orbitals, whereas, in contrast, the HOMO of $[MnFe_3(CO)_{13}C]^-$ does contain manganese atomic orbital character because the manganese and iron 3d atomic orbitals are rather similar in energy.

The Mössbauer effect has been useful in the experimental study of the electronic properties of iron butterfly clusters,[13,15] and the resulting hyperfine spectral parameters have been related to Fenske–Hall molecular orbital results. Specifically, it was found that, as the effective nuclear charge experienced by the iron 4s electrons increases, the s-electron density at the iron nucleus, as probed by the iron-57 isomer shift, increases.[13,15] In this work the electronic properties of a series of homometallic and heterometallic butterfly clusters (see Figure 1) have been investigated through Mössbauer spectroscopy and Fenske–Hall molecular orbital calculations. The isomer shift will be related to the iron 4s Mulliken atomic population and the effective nuclear charge experienced by these electrons. The molecular orbital wave functions will also be used to calculate the electric field gradient at the iron nucleus, and hence the quadrupole splitting, the values of which are then compared with the observed Mössbauer-effect quadrupole splitting.

Experimental Section

The heterometallic butterfly clusters were prepared and characterized by Shriver, Kolis, and Hriljac at Northwestern University.[7-12] The Mössbauer absorbers were prepared under a nitrogen atmosphere in a Vacuum Atmospheres Co. inert-atmosphere glovebox. The Mössbauer spectra were obtained at 78 K on a conventional constant-acceleration spectrometer which utilized a room-temperature rhodium matrix cobalt-57 source and was calibrated at room temperature with natural-abundance α-iron foil. The spectra were fit to symmetric Lorentzian doublets by using standard least-squares computer minimization techniques. The typical error limits are ±0.005 mm/s for the isomer shifts, ±0.01 mm/s for the quadrupole splittings and the line widths, and at most ±1% for the areas.

The molecular orbital calculations were performed by using the Fenske–Hall method.[1,16,17] The atomic basis functions used were those of Herman and Skillman[18] as modified with the Xα to Slater basis program of Bursten and Fenske.[19-21] All of the Fenske–Hall calculations used the same basis functions, and no effort was made to investigate the influence of changes in these functions on the calculated Mössbauer spectral parameters. After considering the structural approximations discussed below and the basis set approximations used, the typical error limits for the absolute metal charges are estimated to be ±0.06. The typical error limits for the absolute carbide and the carbonyl charges and for the metal atomic orbital populations are estimated to be ±0.15 or better. The relative error for a series of compounds is probably a factor of 2 or 3 smaller. A more extensive discussion concerning the error limits of the results of the Fenske–Hall molecular orbital calculations is presented elsewhere.[1]

The atomic positions required for the Fenske–Hall molecular orbital calculations of the homometallic butterfly clusters and of $[RhFe_3(CO)_{12}C]^-$ (IV) were idealized in a fashion similar to that of Harris and Bradley[3] from the known X-ray structures.[11,22-25] The atomic positions of $[MnFe_3(CO)_{13}C]^-$ (VI), $[CrFe_3(CO)_{13}C]^{2-}$ (VII), and $[WFe_3(CO)_{13}C]^{2-}$ (VIII) were based on the structure of $Fe_4(CO)_{13}C$ (V) for the iron atoms, their carbonyl ligands, and the carbide. The atomic positions of $[CrFe_3(CO)_{13}(CH)]^-$ (IX) and $[WFe_3(CO)_{13}(CH)]^-$ (X) were based on the structure of $Fe_4(CO)_{13}C$ (V) for the backbone iron atom, their carbonyl ligands, and the bridging carbonyl ligand and on

(7) Hriljac, J. A.; Harris, S.; Shriver, D. F. *Inorg. Chem.* **1988**, *27*, 816–821.
(8) Hriljac, J. A.; Holt, E. M.; Shriver, D. F. *Inorg. Chem.* **1987**, *26*, 2943–2949.
(9) Stanghellini, P. L.; Sailor, M. J.; Kuznesof, P.; Whitmire, K. H.; Hriljac, J. A.; Kolis, J. W.; Zheng, Y.; Shriver, D. F. *Inorg. Chem.* **1987**, *26*, 2950–2954.
(10) Kolis, J. W.; Holt, E. M.; Hriljac, J. A.; Shriver, D. F. *Organometallics* **1984**, *3*, 496–498.
(11) Hriljac, J. A.; Swepston, P. N.; Shriver, D. F. *Organometallics* **1985**, *4*, 158–166.
(12) Horwitz, C. P.; Holt, E. M.; Shriver, D. F. *Organometallics* **1985**, *4*, 1117–1122.
(13) Benson, C. G.; Long, G. J.; Bradley, J. S.; Kolis, J. W.; Shriver, D. F. *J. Am. Chem. Soc.* **1986**, *108*, 1898–1903.
(14) Levine, I. *Quantum Chemistry*, 3rd ed.; Allyn and Bacon: Boston, MA, 1983; pp 263–265.
(15) Long, G. J.; O'Brien, J. F. *Hyperfine Interact.* **1988**, *40*, 101–110.
(16) Fenske, R. F. *Pure Appl. Chem.* **1971**, *27*, 61–71.
(17) Hall, M. B.; Fenske, R. F. *Inorg. Chem.* **1972**, *11*, 768–775.
(18) Herman, F.; Skillman, S. *Atomic Structure Calculations*; Prentice-Hall: Englewood Cliffs, NJ, 1963.
(19) Bursten, B. E.; Fenske, R. F. *J. Chem. Phys.* **1977**, *67*, 3138–3145.
(20) See instructions provided with the Fenske–Hall code and: Bursten, B. E.; Jensen, R. J.; Fenske, R. F. *J. Chem. Phys.* **1978**, *68*, 3320–3321.
(21) Buhl, M. L.; Long, G. J.; O'Brien, J. F. *Organometallics* **1993**, *12*, 283–288.
(22) Boehme, R. F.; Coppens, P. *Acta Crystallogr., Sect. B.* **1981**, *B37*, 1914–1916.
(23) Bradley, J. S.; Ansell, G. B.; Leonowicz, M. E.; Hill, E. W. *J. Am. Chem. Soc.* **1981**, *103*, 4968–4970.
(24) Holt, E. M.; Whitmire, K. H.; Shriver, D. F. *J. Organomet. Chem.* **1981**, *213*, 125–137.
(25) Beno, M. A.; Williams, J. M.; Tachikawa, M.; Muetterties, E. L. *J. Am. Chem. Soc.* **1981**, *103*, 1485–1492.

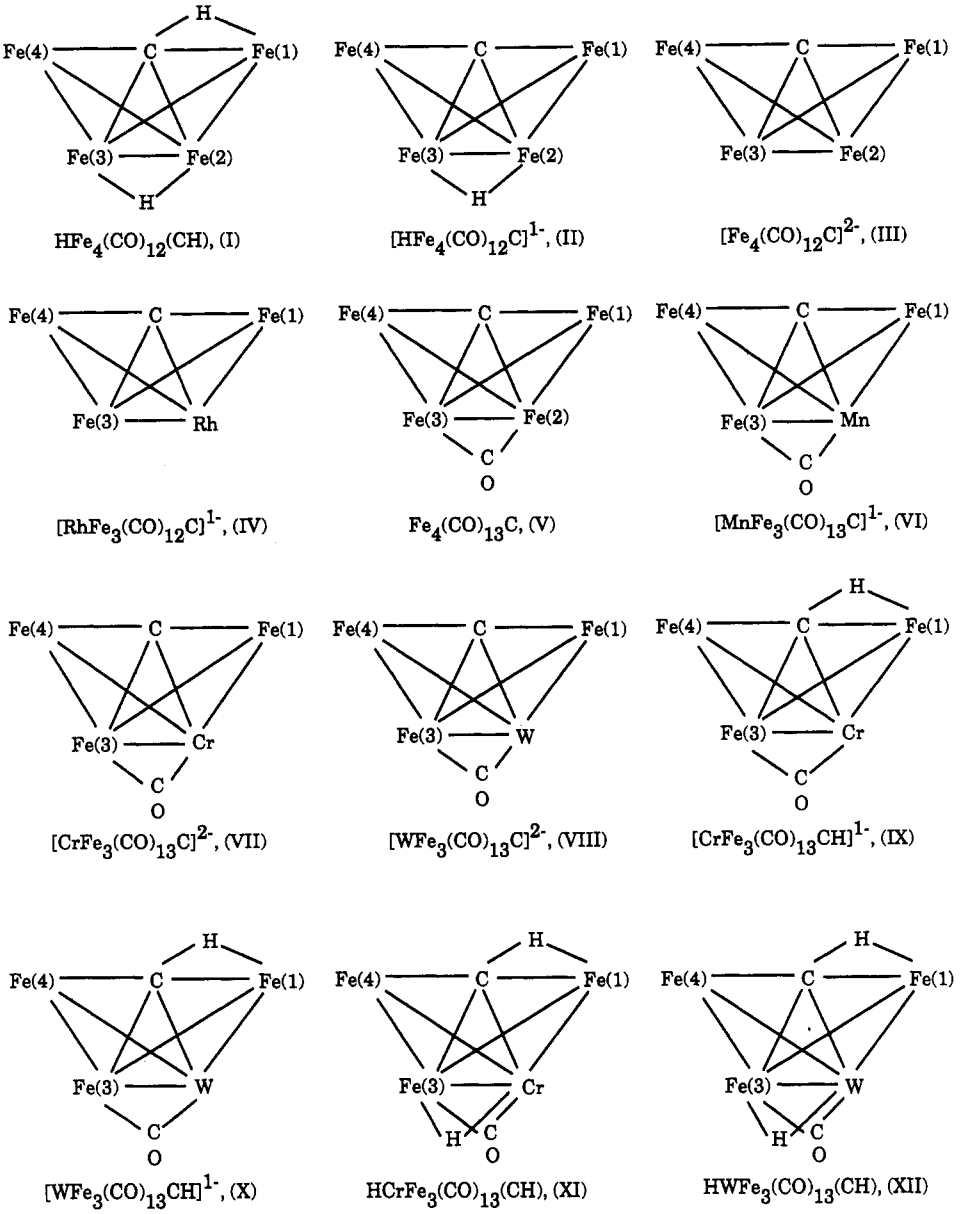

Figure 1. Structures and numbering scheme of the butterfly clusters.

the structure of $HFe_4(CO)_{12}(\eta^2\text{-CH})$ (I) for the wingtip metals, their carbonyl ligands, the carbide, and the bridging hydrogen. The heterometal, in clusters VI–X, was placed on the backbone of the butterfly metal framework at a position which took into account the differences in the metallic radii of the heterometal.[26,27] The positions of the terminal and bridging carbonyl ligands in clusters VI, VII, and IX were the same as those in cluster V, whereas the positions of the tungsten terminal and bridging carbonyl ligands in clusters VIII and X took into account the metallic radii of tungsten. We have investigated the influence of the bridging carbonyl ligand on the Mulliken populations and charges in $Fe_4(CO)_{13}C$ (V). Rotation of the bridging carbonyl by 30° above or below the plane of the backbone iron atoms and the carbide, although it changes the composition of individual molecular orbitals, yields virtually no differences in the populations and charges or the results given in the subsequent discussion. The molecular orbital calculations for $HCrFe_3(CO)_{13}$(CH) (XI) and $HWFe_3(CO)_{13}$(CH) (XII) were not carried out because no X-ray structures or reasonable models were available.

The Mulliken charges and the molecular orbital wave functions, obtained from the Fenske–Hall molecular orbital calculations, were used to calculate[1] the electric field gradient at the metal site. The expectation values $\langle r^{-3}\rangle_{3d}$ and $\langle r^{-3}\rangle_{4p}$ for iron were calculated from the 3d Mulliken orbital populations, whereas those for the other metals were held at the constant values of 32.0 for $\langle r^{-3}\rangle_{3d}$ and 11.6 for $\langle r^{-3}\rangle_{4p}$.[28–30]

Results and Discussion

Mössbauer-Effect Spectra. The Mössbauer spectra for the butterfly clusters studied in this work are shown in Figures 2 and 3, and the derived spectral parameters are given in Table I.[31] Figure 1 shows that the unprotonated heterometallic bufferfly clusters IV and VI–VIII have two chemically inequivalent iron sites, the two wingtip Fe(1,4) atoms and the single backbone Fe(3) atom. The Mössbauer spectra of these clusters are successfully fit with two symmetric quadrupole doublets with equal line widths, one for each inequivalent iron site. The ratio of

(26) The position of the cation, required to calculate the lattice contribution of the metal electric field gradients in clusters VI, IX, and X, was based on the location of the cation in cluster IV. The cation position in clusters VII and VIII was based on that found in cluster III.

(27) Shriver, D. F.; Atkins, P. W.; Langford, C. H. *Inorganic Chemistry*; W. H. Freeman: New York, 1990; p 26.

(28) Trautwein, A.; Harris, F. E.; Dezsi, I. *Theor. Chim. Acta* **1974**, *35*, 231–236.

(29) De Vries, J. L. K. F.; Keijzers, C. P.; De Boer, E. *Inorg. Chem.* **1972**, *11*, 1343–1348.

(30) Weissbluth, M.; Maling, J. E. *J. Chem. Phys.* **1967**, *47*, 4166–4172.

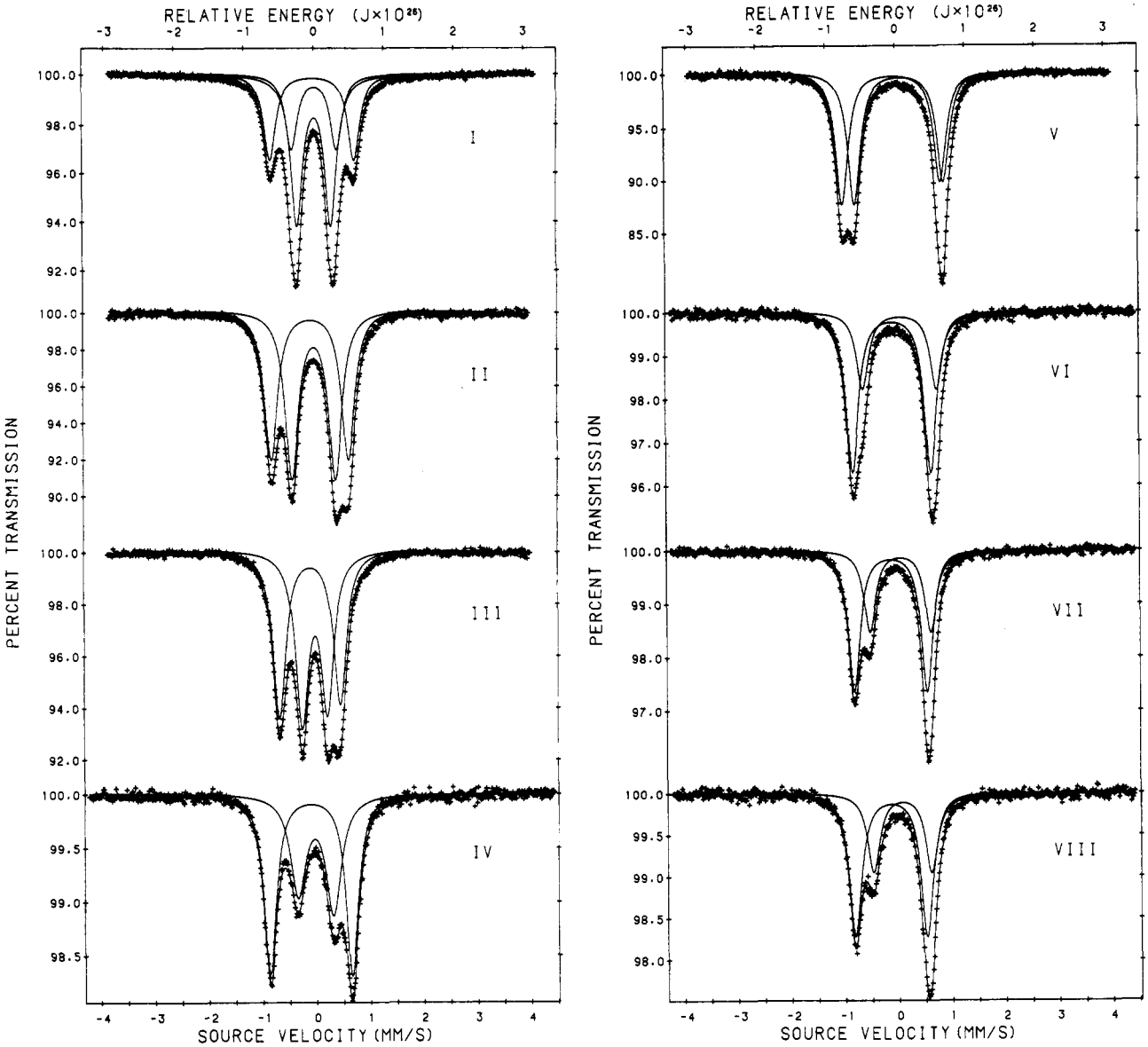

Figure 2. Mössbauer-effect spectra: (A, left) clusters I–IV; (B, right) clusters V–VIII.

the areas of these doublets is unconstrained, and a ratio of approximately 2:1 is observed except for cluster IV, in which Fe(3) has a somewhat higher than expected relative area. The exact reason for this is unclear at this point but may be related to the disorder observed for the backbone metals in this cluster.[11] The assignment of the inner doublet in the spectrum of cluster IV and the right doublet in the spectra of clusters VI–VIII to the backbone iron agrees with the earlier assignments[13] made for the Mössbauer spectral components in $(BzNMe_3)_2[Fe_4(CO)_{12}C]$ (III) and $Fe_4(CO)_{13}C$ (V).

Figure 1 indicates that each of the protonated heterometallic butterfly clusters IX–XII have three chemically inequivalent iron sites. The Mössbauer spectra of these clusters, shown in Figure 3, were therefore fit with three symmetric quadrupole doublets with equal line widths. Table I shows that the areas of the quadrupole doublets of the protonated clusters are very close to the expected ratio of 1:1:1. Because there are three chemically inequivalent iron sites in each of these protonated clusters, the assignment of the components in the spectra is not as straightforward as in the case of the unprotonated clusters. Fortunately, the assignment of the doublets in the spectra of the unprotonated clusters VI–VIII is very useful in assigning the doublets in the spectra of the protonated clusters IX–XII. In the unprotonated clusters, the doublet assigned to the wingtip iron atom has the smallest isomer shift. Therefore, in the spectra of the protonated clusters, the doublet with the smallest isomer shift is assigned to Fe(4), the wingtip iron atom which structurally resembles the wingtip iron atoms in the unprotonated clusters. The assignment of the doublet with the smallest isomer shift to the Fe(4) site is also supported by the coordination number of the iron site. In general a smaller coordination number leads to fewer covalent bonds, reduced covalency, and reduced delocalization of the electron density associated with the metal. The Fe(4) site has the smallest coordination number of the iron sites in the clusters under study, and thus the electron density associated with the Fe(4) site will be more localized, resulting in a smaller isomer shift. This is in agreement with the iron 4s to

(31) The Mössbauer spectral data for the homonuclear iron butterfly clusters I–III and V, in Figures 2 and 3, are from Benson et al.[13] The fits of the data for clusters I–III and V have been changed so that, within each spectrum, the quadrupole doublets have equal line widths. The area ratios of the inner doublets in the spectrum of cluster I have been constrained to 2:1. The doublets of spectra I and II have been reassigned in view of the results of the electric field gradient calculations. The assignments of the doublets in the spectrum of cluster V have been changed to be consistent with those observed herein for the heterometallic clusters.

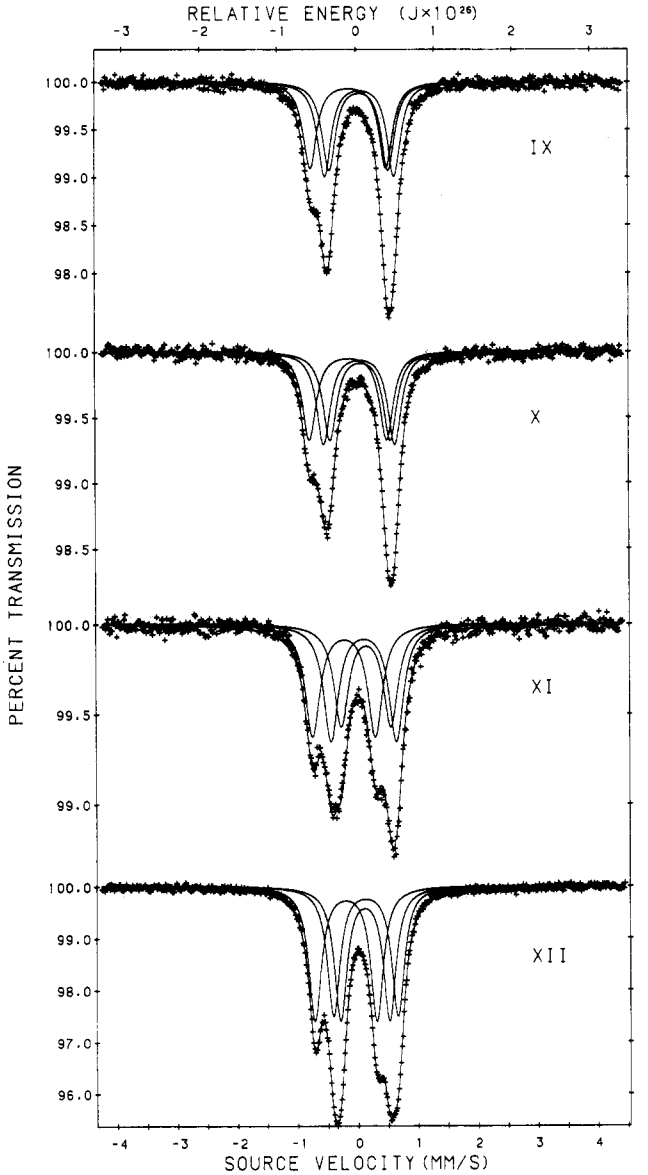

Figure 3. Mössbauer-effect spectra of clusters IX–XII, obtained at 78 K.

near-neighbor overlap populations which will be discussed below. Also, in the spectra of the unprotonated clusters, the doublet assigned to the backbone iron atom has the smallest quadrupole splitting. Therefore, in the spectra of the protonated clusters IX–XII the doublet with the smallest quadrupole splitting is assigned to Fe(3), the backbone iron atom. The remaining doublet is then assigned to Fe(1), the protonated wingtip iron atom. As in previous studies,[13,15] the results of the Fenske–Hall molecular orbital calculations support these assignments.

Solution NMR studies[7] of the monoprotonated tungsten cluster reveal that it exists as a mixture of (PPN)[WFe_3-$(CO)_{13}$(CH)] (X) and (PPN)[$HWFe_3(CO)_{13}$C] (X′). If this mixture existed in the solid state at 78 K, there would be six iron sites, as is shown in Figure 4. The wingtip iron sites labeled as Fe(1), Fe(1′), and Fe(1″) in Figure 4 are chemically equivalent, whereas the iron sites labeled as Fe(2), Fe(3), and Fe(4) are chemically different. These four different iron sites would yield a Mössbauer spectrum consisting of four quadrupole doublets, one of which would be expected to have a significantly larger area. However, this is not observed and we conclude that, in the solid state at 78 K, the cluster exists as the single cluster and not a mixture of the two clusters. The Mössbauer spectra

Table I. Mössbauer-Effect Spectral Parameters[a]

cluster	site[b]	δ[c]	ΔE_Q	Γ	% area
$HFe_4(CO)_{12}(\eta^2$-CH) (I)	$Fe(1)_w$	0.009	0.831	0.26	24.0
	$Fe(4)_w$	−0.029	1.560	0.26	27.9
	$Fe(2,3)_b$	0.005	0.628	0.26	48.1
(PPN)[$HFe_4(CO)_{12}$C] (II)	$Fe(1,4)_w$	−0.092	1.431	0.29	47.4
	$Fe(2,3)_b$	−0.019	0.805	0.29	52.6
$(BzNMe_3)_2$[$Fe_4(CO)_{12}$C] (III)	$Fe(1,4)_w$	−0.110	1.127	0.29	50.0[d]
	$Fe(2,3)_b$	−0.019	0.469	0.29	50.0[d]
(PPN)[$RhFe_3(CO)_{12}$C] (IV)	$Fe(1,4)_w$	−0.105	1.522	0.27	57.3
	$Fe(3)_b$	−0.018	0.658	0.34	42.7
$Fe_4(CO)_{13}$C (V)	$Fe(1,4)_w$	−0.072	1.829	0.28	50.0[d]
	$Fe(2,3)_b$	0.072	1.659	0.28	50.0[d]
(PPN)[$MnFe_3(CO)_{13}$C] (VI)	$Fe(1,4)_w$	−0.090	1.455	0.27	67.5
	$Fe(3)_b$	0.063	1.375	0.27	32.5
$(PPN)_2$[$CrFe_3(CO)_{13}$C] (VII)	$Fe(1,4)_w$	−0.131	1.357	0.26	63.3
	$Fe(3)_b$	0.050	1.134	0.26	36.7
$(PPN)_2$[$WFe_3(CO)_{13}$C] (VIII)	$Fe(1,4)_w$	−0.143	1.340	0.28	64.4
	$Fe(3)_b$	0.068	1.085	0.28	35.6
(PPN)[$CrFe_3(CO)_{13}$CH] (IX)	$Fe(1)_w$	0.063	1.154	0.27	32.1
	$Fe(4)_w$	−0.123	1.256	0.27	35.1
	$Fe(3)_b$	0.051	0.980	0.27	32.7
(PPN)[$WFe_3(CO)_{13}$CH] (X)	$Fe(1)_w$	0.047	1.183	0.27	32.8
	$Fe(4)_w$	−0.138	1.284	0.27	34.4
	$Fe(3)_b$	0.062	1.004	0.27	32.8
$HCrFe_3(CO)_{13}$(CH) (XI)	$Fe(1)_w$	0.103	1.086	0.29	35.4
	$Fe(4)_w$	−0.225	1.040	0.29	34.0
	$Fe(3)_b$	0.141	0.825	0.29	30.6
$HWFe_3(CO)_{13}$(CH) (XII)	$Fe(1)_w$	0.124	1.072	0.25	33.9
	$Fe(4)_w$	−0.205	1.026	0.25	32.7
	$Fe(3)_b$	0.112	0.816	0.25	33.5

[a] Data obtained at 78 K and given in mm/s, except where noted. [b] The wingtip and backbone iron sites are designated by w and b, respectively. [c] The isomer shift is relative to room-temperature natural-abundance α-iron foil. [d] The areas constrained to given values.

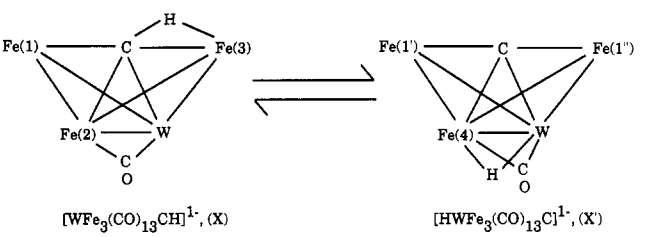

Figure 4. Structure and numbering scheme for a possible mixture of clusters X and X′.

of clusters IX and X are also useful in determining whether the solid-state structure of the cluster is X or X′. As is shown in Figure 4, the backbone-protonated X′ cluster has two inequivalent iron sites and its spectrum should consist of two symmetric quadrupole doublets with a 2:1 area ratio. The doublet with the smallest area, which would also have the smaller isomer shift, must be assigned to the backbone iron atom. However, the backbone iron atom in X′ is also bonded to a bridging proton, which results in a smaller s-electron density at the nucleus and therefore a larger isomer shift. Although the Mössbauer spectrum of X can be fit satisfactorily with two symmetric quadrupole doublets, the assignment of the doublets would be inconsistent with the structure of the backbone-protonated cluster X′. If the solid-state structure is X, then its Mössbauer spectrum would consist of three symmetric quadrupole doublets. When the Mössbauer spectrum of X is fit with three symmetric quadrupole doublets, as shown in Figure 3, the resulting hyperfine parameters are consistent with the structure of the wingtip-protonated structure X. Finally, because the spectra of clusters IX and X are similar, the structures of the clusters are expected to be similar. This further supports the wingtip-protonated cluster (PPN)[$WFe_3(CO)_{13}$(CH)] (X) as the solid-state structure at 78 K.

Table II. Fenske–Hall Molecular Orbital Results

neutral cluster or anion of cluster	site	n	Mulliken atomic orbital population: nd	Mulliken atomic orbital population: $(n+1)s$	Mulliken atomic orbital population: $(n+1)p$	metal charge	av CO terminal charge	ligand	charge	HOMO–LUMO gap	Z_{eff}[a]	Z_{eff}[b]
$HFe_4(CO)_{12}(\eta^2\text{-CH})$ (I)	$Fe(1)_w$	3	6.76	0.34	0.72	+0.17	+0.04	C	−0.56	3.22	3.20	4.74
	$Fe(4)_w$	3	6.75	0.37	0.81	+0.07	+0.02	H	+0.01		3.17	4.74
	$Fe(2)_b$	3	6.74	0.37	0.78	+0.12	+0.03	μ-H	−0.23		3.20	4.76
	$Fe(3)_b$	3	6.72	0.37	0.79	+0.12	+0.01				3.21	4.77
$[HFe_4(CO)_{12}C]^-$ (II)	$Fe(1)_w$	3	6.70	0.37	0.90	+0.02	−0.03	C	−0.58	3.84	3.19	4.78
	$Fe(4)_w$	3	6.70	0.37	0.90	+0.02	−0.03	μ-H	−0.23		3.19	4.78
	$Fe(2)_b$	3	6.72	0.36	0.79	+0.13	−0.05				3.21	4.78
	$Fe(3)_b$	3	6.71	0.36	0.79	+0.13	−0.05				3.21	4.78
$[Fe_4(CO)_{12}C]^{2-}$ (III)	$Fe(1)_w$	3	6.69	0.38	0.92	+0.02	−0.10	C	−0.56	3.33	3.19	4.79
	$Fe(4)_w$	3	6.69	0.38	0.92	+0.02	−0.10				3.19	4.79
	$Fe(2)_b$	3	6.72	0.40	0.88	0.00	−0.15				3.18	4.77
	$Fe(3)_b$	3	6.71	0.40	0.88	0.00	−0.14				3.19	4.77
$[RhFe_3(CO)_{12}C]^-$ (IV)	$Fe(1)_w$	3	6.69	0.37	0.88	+0.06	−0.03	C	−0.51	3.31	3.21	4.79
	$Fe(4)_w$	3	6.67	0.38	0.91	+0.03	−0.08				3.21	4.81
	$Fe(3)_b$	3	6.78	0.38	0.78	+0.05	−0.08				3.16	4.72
	Rh	4	7.46	0.47	1.23	−0.16	+0.03				3.43	
$Fe_4(CO)_{13}C$ (V)	$Fe(1)_w$	3	6.74	0.36	0.83	+0.07	+0.03	C	−0.58	2.95	3.18	4.76
	$Fe(4)_w$	3	6.72	0.37	0.84	+0.07	+0.04	μ-CO	−0.08		3.19	4.77
	$Fe(2)_b$	3	6.78	0.35	0.84	+0.03	+0.05				3.14	4.72
	$Fe(3)_b$	3	6.78	0.35	0.83	+0.04	+0.04				3.15	4.72
$[MnFe_3(CO)_{13}C]^-$ (VI)	$Fe(1)_w$	3	6.72	0.37	0.89	+0.03	−0.04	C	−0.61	2.92	3.18	4.77
	$Fe(4)_w$	3	6.73	0.37	0.87	+0.02	−0.02	μ-CO	−0.17		3.17	4.76
	$Fe(3)_b$	3	6.78	0.35	0.85	+0.02	−0.01				3.14	4.72
	Mn	3	5.87	0.29	0.65	+0.20	−0.09				2.94	4.44
$[CrFe_3(CO)_{13}C]^{2-}$ (VII)	$Fe(1)_w$	3	6.71	0.38	0.93	−0.02	−0.09	C	−0.64	2.78	3.17	4.77
	$Fe(4)_b$	3	6.73	0.38	0.91	−0.02	−0.08	μ-CO	−0.27		3.16	4.76
	$Fe(3)_b$	3	6.78	0.36	0.87	−0.01	−0.06				3.13	4.72
	Cr	3	4.98	0.23	0.45	+0.34	−0.23				2.83	4.28
$[WFe_3(CO)_{13}C]^{2-}$ (VIII)	$Fe(1)_w$	3	6.72	0.38	0.91	0.00	−0.09	C	−0.64	3.06	3.17	4.77
	$Fe(4)_w$	3	6.73	0.38	0.89	0.00	−0.07	μ-CO	−0.27		3.17	4.76
	$Fe(3)_b$	3	6.79	0.35	0.83	+0.04	−0.06				3.14	4.71
	W	5	4.66	0.30	0.68	+0.36	−0.28				3.00	
$[CrFe_3(CO)_{13}CH]^-$ (IX)	$Fe(1)_w$	3	6.77	0.35	0.76	+0.12	−0.02	C	−0.61	2.56	3.18	4.73
	$Fe(4)_w$	3	6.76	0.37	0.85	+0.02	−0.03	H	+0.01		3.16	4.74
	$Fe(3)_b$	3	6.77	0.36	0.87	−0.01	+0.01	μ-CO	−0.22		3.14	4.72
	Cr	3	4.97	0.23	0.47	+0.33	−0.17				2.81	4.27
$[WFe(CO)_{13}CH]^-$ (X)	$Fe(1)_w$	3	6.77	0.35	0.74	+0.14	−0.01	C	−0.61	2.84	3.18	4.73
	$Fe(4)_w$	3	6.76	0.37	0.84	+0.03	−0.02	H	+0.01		3.16	4.74
	$Fe(3)_b$	3	6.78	0.35	0.83	+0.03	+0.01	μ-CO	−0.22		3.14	4.72
	W	5	4.65	0.30	0.69	+0.36	−0.21				3.01	

[a] Effective nuclear charge, experienced by the metal $(n+1)s$ electrons, calculated by using the method of Slater[41,42] and the Mulliken atomic populations. [b] Effective nuclear charge, experienced by the metal $(n+1)s$ electrons, calculated by using the method of Clementi and Raimondi[41] and the Mulliken atomic populations.

Table III. Allred–Rochow Electronegativities and Metallic Radii

atom	electronegativity	metallic radii, Å	atom	electronegativity	metallic radii, Å
H	2.20		Mn	1.60	1.27
C	2.50		Cr	1.56	1.29
O	3.50		W	1.40	1.41
N	3.07		Rh	1.45	1.34
Fe	1.64	1.26			

Fenske–Hall Molecular Orbital Calculations. The results of the Fenske–Hall molecular orbital calculations of the butterfly clusters with 62 cluster electrons are given in Table II. The distribution of the electron density within these clusters and the influence of a proton or a heterometal on this distribution may be understood in terms of the atomic charges. The 12-coordinate metallic radii[27,32] used to determine the bond lengths in heterometallic butterfly clusters VI–X are given in Table III, as are the Allred–Rochow electronegativities[33] of the elements involved in this work. Allred–Rochow electronegativities, which are based on Slater effective nuclear charges and are defined as the electrostatic force exerted by the nucleus on the valence electrons, were found more useful than Pauling's thermochemically based electronegativities.

Harris and Bradley[3] investigated the bonding of the carbide in $[Fe_4(CO)_{12}C]^{2-}$ (III) and found that the carbide donates electron density to the iron atoms of the butterfly framework. The interaction between the carbide $2p_x$ and $2p_z$ orbitals and the backbone iron atomic orbitals were found to be σ-bonding, whereas the carbide $2p_x$ and $2p_z$ to wingtip iron interactions were π-bonding. The carbide $2p_y$ atomic orbital interacts only with the wingtip iron through σ-bonding. The major carbide 2p to iron 3d overlap population was located between the carbide $2p_y$ and the iron wingtip 3d atomic orbitals. In agreement with the calculations of Harris and Bradley[3,13] on clusters II, III, and V, we also find that the carbide 2p to wingtip iron overlap populations of the unprotonated clusters II–VIII are about twice as large as the carbide 2p to backbone iron overlap populations. Both in our work and in that of Harris and Bradley, this may be attributed[3] to the shorter carbide to wingtip iron bond lengths, which range from 1.72 Å in cluster IV to 1.80 Å in cluster III, as

(32) Metallic radii were chosen because these clusters are used as models of metal surfaces. The sum of two iron metallic radii, 2.52 Å, is similar to the iron–iron backbone bond length found in these clusters, which ranges from 2.53 Å in cluster III to 2.61 Å in cluster II. The sum of the iron and heterometal metallic radii is also similar to the iron–heterometal backbone bond length used in the structures of these clusters. The iron wingtip to backbone bond lengths are at most 0.2 Å larger than the sum of two iron metallic radii.

(33) Huheey, J. E. *Inorganic Chemistry: Principles of Structure and Reactivity*, 3rd ed.; Harper and Row: New York, 1983; pp 141–149.

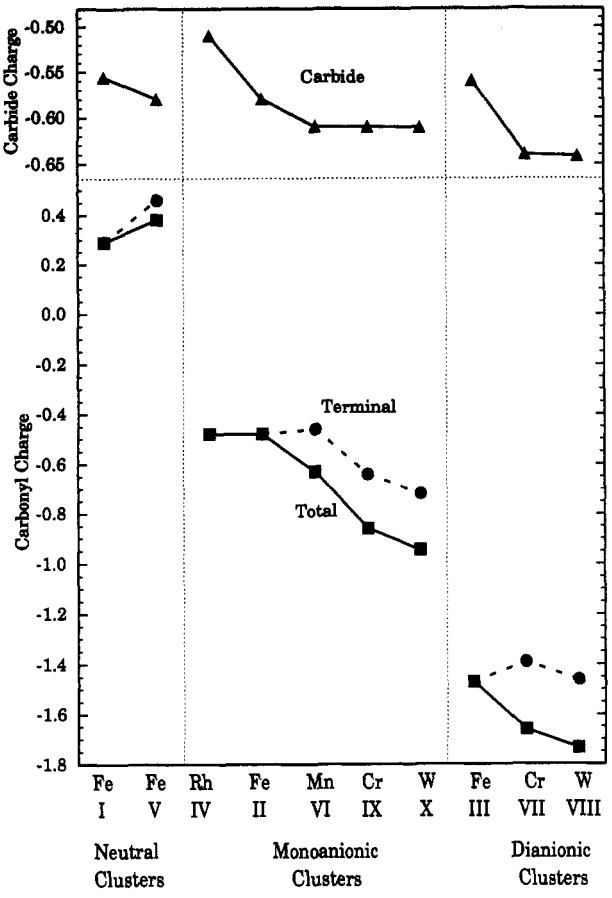

Figure 5. Carbide charge (▲), total terminal carbonyl charge (●), and total carbonyl ligand charge (■). In this and other figures the M(2) metal is indicated at the bottom of the figure.

compared to those of the carbide to backbone iron, which range from 1.96 Å in cluster III to 2.12 Å in cluster IV.

The nearly constant carbide charge of ca. −0.6 in the clusters is shown at the top of Figure 5. This value agrees well with the average of −0.64, found by Harris and Bradley[3,13,34] for clusters II, III, and V. The similarity in the metal environment of the carbide, as it serves as a Lewis base and donates electron density to the metals, yields the essentially constant negative carbide charge. However, differences between the carbide charge found in the wingtip-protonated clusters I, IX, and X and that found in the wingtip-unprotonated clusters with the same M(2) atom III, VII, and VIII can be seen in Figure 5. When the carbide is protonated, as in I, IX, and X, it shares electron density with hydrogen and becomes slightly less negative than in the unprotonated clusters III, VII, and VIII. Also, whereas the average backbone M(2,3) to carbide bond lengths of 1.97 Å in the protonated and 1.99 Å in the unprotonated clusters are similar, the differences between the average wingtip Fe(1,4) to carbide bond length of 1.88 Å in the protonated and 1.79 Å in the unprotonated clusters may influence the carbide charge. As the average wingtip iron to carbide bond length increases, the average iron–carbide overlap population decreases, and the carbide charge of the wingtip-protonated clusters becomes less negative than in the unprotonated clusters with the same M(2) atom. As shown in Figure 5, the carbide charge in cluster IV is somewhat higher than the other carbide charges. The higher value may be attributed to the smaller electronegativity of rhodium as compared with that of the other metals (see Table III). Although the 1.77-Å average wingtip iron to carbide bond length[11] in cluster IV is similar to the 1.79-Å average value in the unprotonated clusters, the 2.09-Å average backbone metal to carbide bond length is larger than the 1.99-Å average in the other unprotonated clusters, a difference which may account for the higher carbide charge.

(34) The charges given in Table II for clusters II, III, and V do not agree exactly with those reported by Harris and Bradley[3,13] because different basis sets were used.

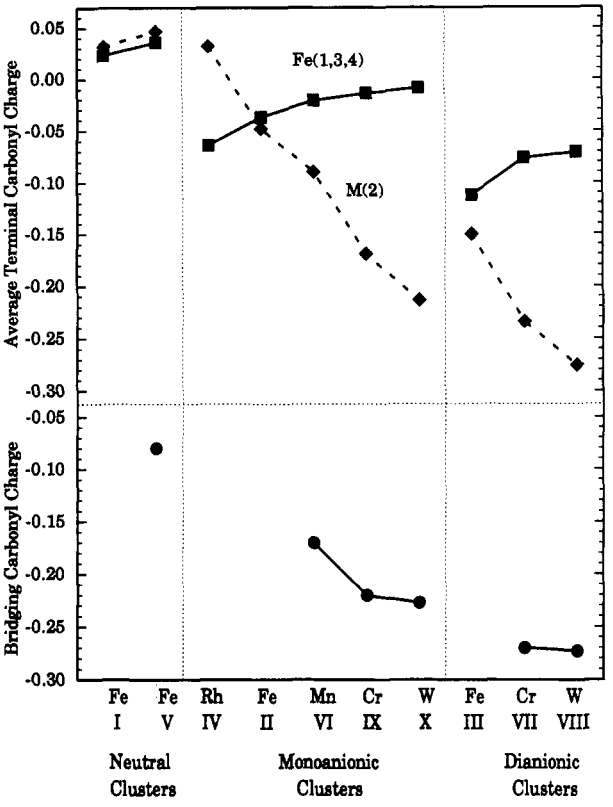

Figure 6. Average Fe(1,3,4) terminal carbonyl charge (■), average M(2) terminal carbonyl charge (◆), and bridging carbonyl charge (●).

The protonation of the heterometallic clusters VII and VIII, to form clusters IX and X, occurs across the carbide and wingtip iron atoms. In contrast, protonation[3] of cluster III occurs across the backbone iron atoms. The frontier orbitals of VII and VIII, which contain metal and backbone iron character, are already used for bonding by the bridging carbonyl and are therefore unavailable for protonation. As a result, the protonation of clusters VII and VIII occurs across the carbide and the wingtip iron. This agrees with the results of Hriljac et al.,[7] in which the protonation of $[MnFe_3(CO)_{13}C]^-$ (VI) also occurred across the carbide and the wingtip iron.

The total carbonyl charge in the clusters is shown in Figure 5, which reveals that the carbonyl charge depends more upon the anionic cluster than the heterometal found in a cluster. As the anionic charge increases, an increasing portion of the electron density distributes itself onto the carbonyl ligands, a distribution which yields the maximum charge separation and minimum interelectronic repulsion. The approximate unit decrease in the carbonyl charge in each of the monoanionic and dianionic clusters reveals that the additional anionic charge is almost completely dispersed onto the carbonyl ligands.

The distribution of the additional anionic charge onto the carbonyl ligands of the iron or the heterometal is shown in Figure 6. The largest portion of the additional anionic charge is found on the carbonyl ligands bonded to the heterometal. The average terminal carbonyl ligand charge in the neutral clusters is very close to zero, indicating, as

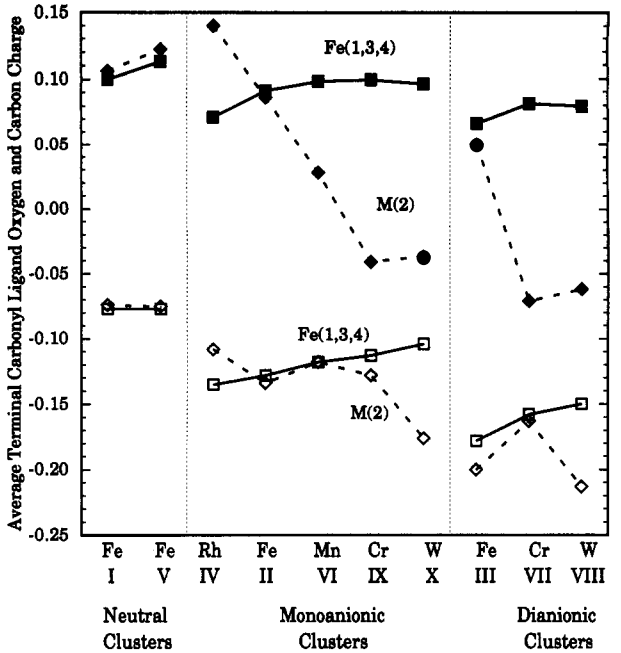

Figure 7. Average Fe(1,3,4) terminal carbonyl carbon charge (■), average M(2) terminal carbonyl carbon charge (◆), average Fe(1,3,4) terminal carbonyl oxygen charge (□), and average M(2) terminal carbonyl oxygen charge (◇).

expected, little electron delocalization onto the carbonyl ligands. In the monoanionic and dianionic clusters, with the exception of cluster IV, the average M(2) terminal carbonyl ligand charge is more negative than that of the remaining three iron sites, Fe(1,3,4). In these clusters, the carbonyl ligand behaves as a Lewis base and the carbon donates electron density to the metal. However, when an iron is replaced by a heterometal with a smaller electronegativity, the heterometal accepts less electron density from its carbonyl ligands, and as a result, the carbonyl ligand charge is more negative. As mentioned above and shown in Figure 6, the average charge of the rhodium carbonyl ligands in cluster IV is less negative than that of the remaining iron sites. This difference shows the influence of the metal to carbonyl ligand carbon bond length upon the carbonyl ligand charge. With the exception of cluster IV, the average backbone M(2) to carbonyl ligand carbon bond length is 1.79 Å. In contrast, in IV this bond length is 1.88 Å. As the backbone M(2) to carbonyl ligand carbon bond length increases, the metal–ligand overlap population decreases, and the carbonyl ligand charge becomes less negative.

Table II and Figure 6 indicate that the bridging hydrogen and carbonyl ligands also accept a small portion of the additional anionic charge. In clusters I and II, the bridging hydrogen near-neighbor environment does not change and neither does its charge. As for the terminal carbonyl ligand charges, the bridging carbonyl ligand charge becomes more negative as the electronegativity of the heterometal decreases.

The carbon and oxygen charges of the terminal carbonyl ligands are shown in Figure 7. It is the more electronegative oxygen of the carbonyl ligands which accepts the additional anionic charge and which also allows for the greatest charge separation. The charges of the carbon atoms bonded to iron are positive and are nearly constant. In contrast, the charge of the carbon bonded to the heterometal becomes more negative as the electronegativity of M(2) decreases.

Carbonyl ligands serve as models[35,36] of chemisorbed carbon monoxide on a metal surface. It has been proposed[37] that the electronic structure of the cluster terminal carbonyl ligands is relatively unchanged from that in carbon monoxide. The validity of this proposal can be tested by a comparison of the molecular orbitals of carbon monoxide with those of the iron-bonded terminal carbonyl ligands. A carbon monoxide molecule, which has a bond length of 1.128 Å, has a carbon charge of −0.095, an oxygen charge of +0.095, and a carbon–oxygen overlap population of 1.57. A carbon monoxide molecule with a bond length of 1.14 Å, as in the typical average carbonyl ligand, was found to have a carbon charge of −0.085, an oxygen charge of +0.085, and a carbon–oxygen overlap population of 1.56. For the terminal carbonyl ligands in these clusters, the average carbonyl carbon charge is 0.09, the average carbonyl oxygen charge is −0.13, and the average carbonyl carbon–oxygen overlap population is 1.50. A more detailed look at the carbon–oxygen overlap populations of both carbon monoxide and the carbonyl ligand is presented in Table IV. As the carbonyl carbon donates electron density to the metal, the carbonyl carbon 2p to oxygen 2p overlap population decreases as compared to that of carbon monoxide. The increase in the carbonyl carbon 2s to oxygen 2p overlap population, as compared to that of carbon monoxide, may be due to the delocalization of the metal electron density which the carbonyl ligand carbon 2p orbital accepts through π back-bonding. Overall, the carbonyl ligand carbon–oxygen overlap population is similar to that of carbon monoxide, and thus their overall electronic properties are similar. It would appear that the small differences in the specific carbon–oxygen orbital overlap populations make carbonyl ligands useful models for chemisorbed carbon monoxide on a metal surface.

Table IV. Comparison of the CO and Carbonyl Ligand Overlap Populations

species	CO bond length, Å	oxygen orbital	C, 2s	C, 2p	C, total
CO	1.128	O, 2s	0.21	0.18	0.39
		O, 2p	0.03	1.15	1.18
		O, total	0.24	1.33	1.57
CO	1.14[a]	O, 2s	0.20	0.18	0.38
		O, 2p	0.04	1.14	1.18
		O, total	0.24	1.32	1.56
carbonyl ligand[a]	1.14	O, 2s	0.16	0.23	0.39
		O, 2p	0.24	0.87	1.11
		O, total	0.40	1.10	1.50

[a] The average of the 120 terminal carbonyl ligands.

The metal charges in the butterfly clusters are given in Table II. In agreement with the calculations of Harris and Bradley[3,13] on $[HFe_4(CO)_{12}C]^-$ (II), the backbone Fe(2,3) charges are found to be more positive than the wingtip Fe(1,4) charges. The backbone iron atoms share their electron density with the bridging hydrogen, which results in the more positive backbone iron charge. Also in agreement with the calculations of Harris and Bradley,[3,13] the wingtip Fe(1,4) charges of clusters III and V were found to be more positive than the backbone Fe(2,3) charges. Figure 8 shows that the protonated Fe(1) in I, IX, and X has an average charge of +0.14 and range of +0.12 to +0.17 and that the remaining iron atoms have a smaller average charge of +0.04 and range of −0.02 to +0.13. It appears that these charges are, as expected, rather independent of the nature and charge of the M(2) heterometal. When

(35) Muetterties, E. L.; Rhodin, T. N.; Band, E.; Brucker, C. F.; Pretzer, W. R. *Chem. Rev.* **1979**, *79*, 91–137.
(36) Somorjai, G. A. *Science* **1985**, *227*, 902–908.
(37) Huheey, J. E. *Inorganic Chemistry: Principles of Structure and Reactivity*, 3rd ed.; Harper and Row: New York, 1983; p 592.

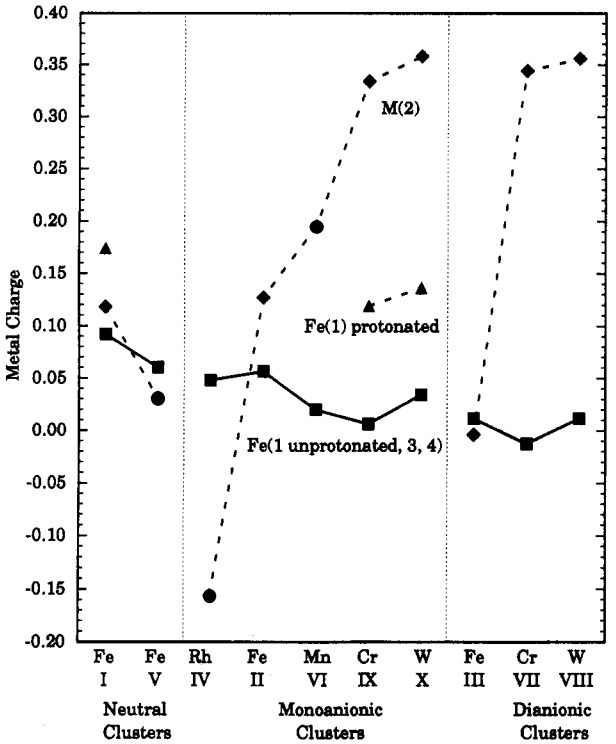

Figure 8. Average unprotonated wingtip Fe(1,4) and backbone Fe(3) charge (■), protonated wingtip Fe(1) charge (▲), and M(2) backbone charge (◇).

the wingtip Fe(1) is protonated, as in I, IX, and X, it shares its electron density with hydrogen, and its charge becomes somewhat more positive than those of the remaining iron atoms. M(2) shows by far the largest range of charges which are related to the environment and the kind of metal. As the electronegativity of M(2) decreases, it attracts less electron density from the carbonyl ligands and consequently has a more positive charge. The close relationship between the carbonyl ligand charge and the metal charge may be seen in a comparison of Figures 6–8.

The effect of the heterometal on the iron charge is illustrated by the replacement of the Fe(2) atom in $Fe_4(CO)_{13}C$ (V) with a manganese, chromium, or tungsten atom, in clusters VI–VIII. As shown in Figure 9, the decrease in the iron charge can, in part, be attributed to differences in the electronegativity of the heterometal and iron. Because manganese and chromium are less electronegative than iron, in their presence the remaining iron atoms attract relatively more electron density and thus become more negative. However, this trend is not observed for tungsten in VIII, apparently because the iron charges in cluster VIII are influenced by the metal–metal bond lengths. In clusters V–VII, the average wingtip iron to M(2) bond length is 2.64 Å and the average backbone iron to M(2) bond length is 2.54 Å. In contrast, in VIII the wingtip iron to tungsten bond length is 2.71 Å and the backbone iron to tungsten bond length is 2.68 Å. These increased bond lengths decrease the iron–tungsten overlap populations, decrease the iron orbital populations, and increase the iron charge.

The average iron 3d, 4s, and 4p and the M(2) *n*d, (*n* + 1)s, and (*n* + 1)p Mulliken atomic orbital populations are shown in Figure 10. The iron 4s atomic orbital populations are virtually constant at ca. 0.37 e. This value agrees rather well[34] with the average 0.41-e value found by Harris and Bradley[3,13] for clusters II, III, and V. The overlap populations between the iron 4s atomic orbitals and the carbide are on average 0.10 with a range of 0.05–0.14,

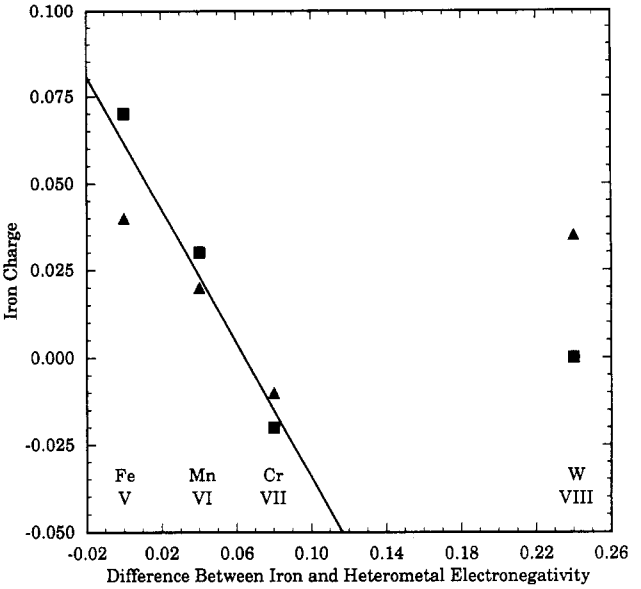

Figure 9. Wingtip Fe(1,4) (■) and backbone Fe(3) (▲) charge versus the difference in the Allred–Rochow electronegativity of the metals.

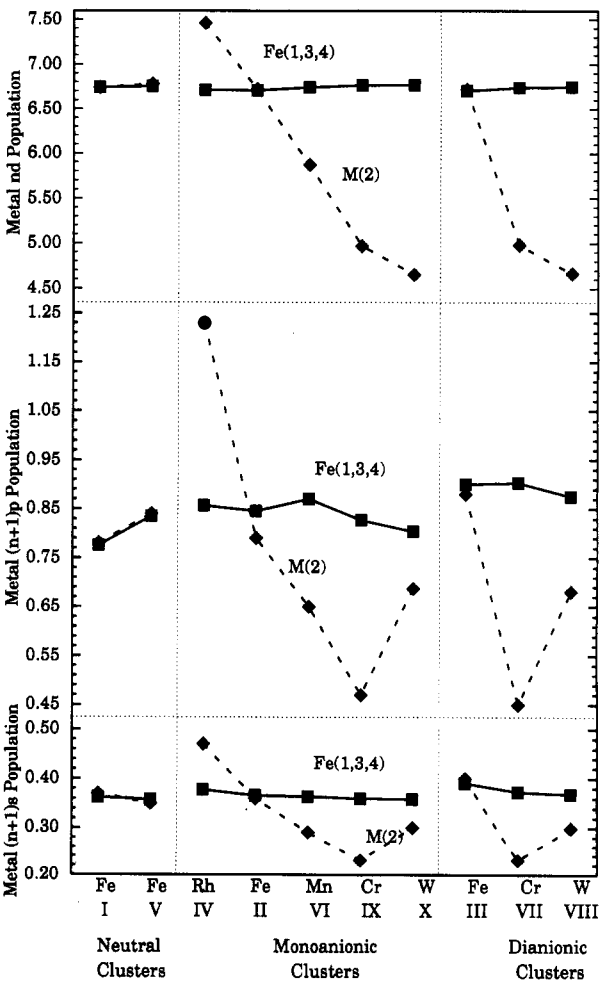

Figure 10. Average of the iron (■) and the M(2) (◆) Mulliken atomic orbital populations.

whereas with the carbonyl ligand carbon the overlap is on average 0.15 with a range of 0.14–0.18. In contrast, the metal–metal s–orbital overlap population of –0.01 is negligible. Because the range of these overlap populations is small, the iron 4s atomic orbital populations remain rather constant, as do also the iron 3d populations. The major variation in iron orbital populations occurs in the

iron 4p orbitals. The major metal–metal framework bonding occurs between the metal *n*d and (*n* + 1)p atomic orbitals. The iron 3d and 4p atomic orbital populations are determined by both their overlap populations and the carbide and carbonyl ligand charges. The iron 4p to metal overlap populations are smaller than the iron 3d to metal overlap populations, indicating that the 4p orbitals interact less effectively with their near-neighbor metals than do the iron 3d orbitals. As a result, the carbide and carbonyl ligand charges have a greater influence on the iron 4p than on the iron 3d population. The greater influence of the carbonyl ligand charge on the iron 4p populations is revealed by a comparison of Figures 5 and 10. The backbone M(2) populations also depend upon the carbide and carbonyl ligand charges. The M(2) (*n* + 1)s and (*n* + 1)p populations are mainly determined by the bridging carbonyl ligand charge, whereas, in contrast, the *n*d populations are more sensitive to the average terminal carbonyl ligand charge.

Mössbauer-Effect Isomer Shift. The results of the Fenske–Hall molecular orbital calculations, given in Table II, may be used to understand the variations in the Mössbauer-effect isomer shifts. As the s-electron density at the iron nucleus decreases, the iron-57 isomer shift increases. Therefore, it is expected that, as the iron 4s Mulliken population increases, the isomer shift will decrease. A linear fit[21] of the isomer shifts versus the iron 4s Mulliken atomic orbital populations of several series of clusters[13,15,38–40] has a slope of −1.50 (mm/s)/e, an intercept of 0.53 mm/s, and a correlation of 0.81. The poor correlation results, in part, because the 4s Mulliken atomic populations do not take into account any shielding from the 3d and 4p electrons. In previous work,[13,15] these shielding effects were considered by calculating the Slater effective nuclear charge experienced by the iron 4s electrons. As the effective nuclear charge experienced by the iron 4s electrons increases, the 4s electrons are drawn closer to the nucleus, the s-electron density at the nucleus increases, and the isomer shift decreases. A better estimate of the effective nuclear charge experienced by the iron 4s electrons can be obtained by using the Clementi and Raimondi[41] effective nuclear charges. Clementi and Raimondi used self-consistent-field wave functions to determine the nuclear shielding produced by different types of electrons. Both the Slater and the Clementi and Raimondi effective nuclear charges, Z_{eff}, experienced by the iron 4s electrons were calculated from the iron Mulliken populations,[41,42] and the resulting values are given in Table II. The Clementi and Raimondi effective nuclear charge experienced by a free isolated iron 4s electron with an electronic configuration of $4s^2 3d^6 4p^0$ is 5.434.[41] The average effective nuclear charge experienced by the iron 4s electrons in the butterfly clusters is 4.75, a value considerably smaller than in the isolated atom. In these clusters it is the iron to carbide and carbonyl ligand carbon overlap which increases the iron 3d and 4p orbital populations and decreases the iron 4s orbital population, thereby leading to a larger screening constant for the iron 4s electrons and a smaller effective nuclear charge.

A better representation of the s-electron density at the iron nucleus may be obtained by considering both the iron 4s Mulliken population and the effective nuclear charge experienced by the iron 4s electrons. Figure 11, which includes the clusters in this and related work,[13,15,38–40] shows the sum of the iron 4s Mulliken population and the Clementi and Raimondi effective nuclear charge experienced by the iron 4s electrons versus the iron-57 isomer shift. A linear fit of these values has a slope of −0.88 (mm/s)/e, an intercept of 4.77 mm/s, and a correlation of 0.86. Although the correlation is far from perfect, the expected trend is clearly observed. The relationship illustrated in Figure 11 may be expressed as

$$\delta = m[c_1(n_{4s}) + c_2(Z_{eff})] + b \qquad (1)$$

where m is the slope with units of (mm/s)/e and b is the δ intercept in mm/s. The constants c_1 and c_2 represent the relative influence on the isomer shift of the iron 4s population and the effective nuclear charge, respectively.[43] For the fit shown in Figure 11, the constants have values of −1.0 for c_1 and −1.0 e/proton for c_2.

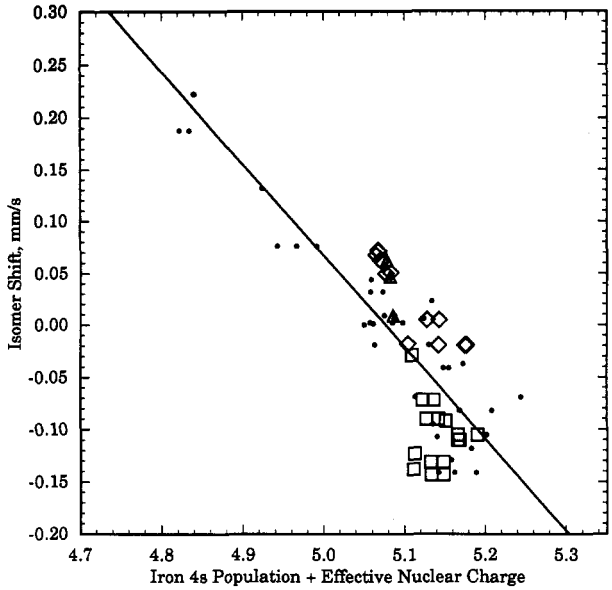

Figure 11. Iron-57 isomer shift versus the sum of the iron 4s Mulliken atomic population and the Clementi and Raimondi effective nuclear charge experienced by the iron 4s electrons for the unprotonated wingtip iron (□), the protonated wingtip iron (△), and the backbone iron (◇). The smaller points represent values obtained for a variety of related clusters (see text for references).

Figure 11 shows that the isomer shift values are divided into two groups, indicating that there are two rather different environments at the iron nuclei in these clusters. The more positive isomer shifts correspond to both the protonated wingtip Fe(1) and the backbone Fe(2,3) sites. The more negative isomer shifts correspond to the unprotonated wingtip Fe(1,4) sites. This indicates that the s-electron density at the nucleus of the protonated wingtip and backbone iron atoms is less than at the unprotonated wingtip iron atoms. These differences arise from different iron 4s overlap populations. The average iron 4s to metal overlap population is −0.01, and the average protonated iron 4s to hydrogen overlap population is −0.03. Hence, these overlaps do not significantly influence the s-electron density of the iron. The major iron 4s overlap

(38) Benson, C. G.; Long, G. J.; Kolis, J. W.; Shriver, D. F. *J. Am. Chem. Soc.* **1985**, *107*, 5297–5298.
(39) Buhl, M. L.; Long, G. J. *J. Organomet. Chem.*, in press.
(40) Buhl, M. L.; Long, G. J.; Doyle, G. *J. Organomet. Chem.*, in press.
(41) Huheey, J. E. *Inorganic Chemistry: Principles of Structure and Reactivity*, 3rd ed.; Harper and Row: New York, 1983; pp 37–38.
(42) Slater, J. C. *Phys. Rev.* **1930**, *36*, 57–64.

(43) By solving eq 1 for the values of c_1 and c_2 which yield the best correlation with the isomer shift, we obtain a slope of −1.0 (mm/s)/e, an intercept for 4.17 mm/s, a value of 0.98 for c_1, and a value of 0.81 e/proton for c_2. This indicates that, as expected, the effective nuclear charge has a smaller influence on the isomer shift than does the iron 4s orbital population.

Table V. Comparison of the Observed and Calculated Quadrupole Splittings[a]

			calc total			calc valence					calc lattice			
cluster	site	obs ΔE_Q	ΔE_Q	V_{zz}	η	ΔE_Q	V_{zz}	η	$\langle r^{-3}\rangle_{3d}$	%	ΔE_Q	V_{zz}	η	%
$HFe_4(CO)_{12}(\eta^2\text{-CH})$ (I)	$Fe(1)_w$	0.831	1.64	0.79	0.08	1.68	0.81	0.08	31.3	97	−0.05	−0.02	0.16	3
	$Fe(4)_w$	1.560	1.73	0.79	0.58	1.71	0.78	0.59	31.3	99	−0.06	−0.03	0.13	1
	$Fe(2)_b$	0.628	0.96	0.44	0.54	0.43	0.93	0.52	31.4	97	0.04	0.02	0.61	3
	$Fe(3)_b$	0.628	0.68	0.30	0.70	0.68	0.30	0.67	31.4	99	0.04	0.02	0.61	1
$(PPN)[HFe_4(CO)_{12}]$ (II)	$Fe(1)_w$	1.431	1.37	0.65	0.32	1.41	0.67	0.29	31.5	97	−0.07	−0.03	0.14	3
	$Fe(4)_w$	1.431	1.37	0.65	0.32	1.41	0.67	0.29	31.5	97	−0.07	−0.03	0.15	3
	$Fe(2)_b$	0.805	0.88	0.42	0.23	0.89	0.43	0.18	31.5	99	0.04	0.02	0.76	1
	$Fe(3)_b$	0.805	0.89	0.42	0.23	0.89	0.43	0.18	31.5	99	0.04	0.02	0.92	1
$(BzNMe_3)_2[Fe_4(CO)_{12}C]$ (III)	$Fe(1)_w$	1.127	1.18	0.52	0.75	1.22	0.54	0.72	31.6	96	−0.06	−0.03	0.08	4
	$Fe(4)_w$	1.127	1.25	0.57	0.59	1.30	0.59	0.57	31.5	96	−0.06	−0.03	0.25	4
	$Fe(2)_b$	0.469	0.71	0.30	0.95	0.68	0.29	0.91	31.5	95	−0.05	−0.02	0.09	5
	$Fe(3)_b$	0.469	−0.79	−0.34	0.83	−0.76	−0.32	0.88	31.5	96	−0.04	−0.02	0.10	4
$(PPN)[RhFe_3(CO)_{12}C]$ (IV)	$Fe(1)_w$	1.522	1.42	0.60	0.96	1.46	0.62	0.92	31.6	97	−0.06	−0.03	0.13	3
	$Fe(4)_w$	1.522	1.27	0.60	0.39	1.31	0.61	0.40	31.6	97	−0.09	−0.04	0.92	3
	$Fe(3)_b$	0.658	−0.34	−0.15	0.81	0.36	0.15	0.89	31.2	97	−0.06	−0.03	0.98	3
	Rh			−0.32	0.20		−0.32	0.31	32.0			−0.02	0.93	
$Fe_4(CO)_{13}C$ (V)	$Fe(1)_w$	1.829	1.50	0.72	0.10	1.46	0.70	0.07	31.4	98	−0.07	−0.03	0.06	2
	$Fe(4)_w$	1.829	1.61	0.77	0.17	1.65	0.79	0.16	31.4	98	−0.07	−0.03	0.05	2
	$Fe(2)_b$	1.659	1.40	0.66	0.40	1.38	0.65	0.42	31.2	99	−0.05	−0.02	0.18	1
	$Fe(3)_b$	1.659	1.25	0.60	0.04	1.26	0.61	0.07	31.1	99	−0.05	−0.02	0.16	1
$(PPN)[MNFe_3(CO)_{13}C]$ (VI)	$Fe(1)_w$	1.455	1.52	0.69	0.61	1.47	0.67	0.58	31.4	97	−0.07	−0.03	0.10	3
	$Fe(4)_w$	1.455	1.60	0.76	0.31	1.64	0.78	0.31	31.3	97	−0.07	−0.03	0.11	3
	$Fe(3)_b$	1.375	0.94	0.42	0.62	0.93	0.42	0.61	31.2	99	−0.05	−0.02	0.43	1
	Mn			0.68	0.25		0.66	0.27	32.0			−0.03	0.52	
$(PPN)_2[CrFe_3(CO)_{13}C]$ (VII)	$Fe(1)_w$	1.357	−1.70	−0.73	0.89	−1.66	−0.71	0.89	31.5	97	−0.07	−0.03	0.07	3
	$Fe(4)_w$	1.357	1.74	0.76	0.81	1.80	0.79	0.79	31.4	97	−0.10	−0.04	0.49	3
	$Fe(3)_b$	1.134	−0.72	−0.35	0.19	−0.73	−0.35	0.20	31.2	99	−0.05	−0.02	0.46	1
	Cr			0.74	0.15		0.72	0.17	32.0			−0.03	0.92	
$(PPN)_2[WFe_3(CO)_{13}C]$ (VIII)	$Fe(1)_w$	1.340	1.70	0.71	0.97	1.65	0.69	0.96	31.4	97	−0.07	−0.03	0.09	3
	$Fe(4)_w$	1.340	1.73	0.77	0.68	1.79	0.80	0.66	31.4	97	−0.09	−0.04	0.51	3
	$Fe(3)_b$	1.085	−0.86	−0.39	0.38	−0.87	−0.39	0.68	31.2	99	−0.05	−0.02	0.46	1
	W			0.67	0.26		0.65	0.23	32.0			−0.03	0.87	
$(PPN)[CrFe_3(CO)_{13}CH]$ (IX)	$Fe(1)_w$	1.154	−1.98	−0.83	0.96	−1.97	−0.82	0.98	31.2	99	−0.05	−0.03	0.11	1
	$Fe(4)_w$	1.256	1.77	0.77	0.83	1.80	0.78	0.82	31.3	98	−0.06	−0.03	0.16	2
	$Fe(3)_b$	0.980	−0.83	−0.38	0.53	−0.85	−0.39	0.61	31.2	97	−0.05	−0.03	0.28	3
	Cr			0.79	0.61		0.78	0.66	32.0			−0.02	0.44	
$(PPN)[WFe_3(CO)_{13}CH]$ (X)	$Fe(1)_w$	1.183	1.90	0.81	0.89	1.89	0.81	0.86	31.2	99	−0.05	−0.03	0.13	1
	$Fe(4)_w$	1.284	1.80	0.78	0.83	1.83	0.80	0.82	31.3	99	−0.06	−0.03	0.19	1
	$Fe(3)_b$	1.004	−0.95	−0.44	0.39	−0.97	−0.45	0.46	31.2	98	−0.05	−0.02	0.26	2
	W			0.72	0.22		0.71	0.26	32.0			−0.02	0.52	

[a] The ΔE_Q values were obtained at 78 K and have units of mm/s. V_{zz} values have units of V/m^2 and must be multiplied by 10^{22}.

is with the carbide and the carbonyl carbon atomic orbitals. The average 0.16 iron 4s to terminal carbonyl carbon overlap population is similar for both the wingtip and the backbone iron atoms. It is the iron 4s to carbide overlap population which has the greatest influence on the s-electron density at the iron nucleus. The backbone and protonated iron 4s to carbide average overlap population of 0.06 is less than the unprotonated wingtip iron 4s to carbide value of 0.12. Thus, in agreement with the isomer shift, the 4s electron densities at the nuclei of the backbone and protonated wingtip iron atoms are less than for the unprotonated wingtip iron. The isomer shifts of the backbone and protonated wingtip iron atoms are similar because of the similarity in their iron 4s to carbide overlap populations. The isomer shifts of the backbone iron atoms with a bridging carbonyl ligand are more positive than those without the bridging carbonyl ligand, indicating less s-electron density in the former case. This is surprising because the iron 4s to bridging carbonyl ligand overlap population of 0.05 indicates that the bridging carbonyl ligands donate electron density to the iron 4s atomic orbitals.

Mössbauer-Effect Quadrupole Interaction. The valence, lattice, and total electric field gradients, calculated from the molecular orbital wave function coefficients and the Mulliken charges, are given in Table V. The nonintegral nonequivalent atomic populations of the iron 3d and 4p atomic orbitals lead to the dominance of the valence contribution over that of the lattice contribution to the electric field gradient in these clusters. The experimental and calculated values of ΔE_Q are compared in Figure 12, which also presents results for several related series of clusters.[13,15,38-40] Because the Mössbauer effect yields only the magnitude of ΔE_Q, the sign of the calculated value was assigned to the experimental value. Figure 12 shows that the Fenske–Hall molecular orbital calculations are rather successful in predicting the electric field gradients in these clusters. For example, as expected, the calculated quadrupole splittings of the wingtip iron atoms are greater than those of the backbone iron atoms. Also, in general, the backbone iron atoms with bridging ligands have a greater calculated quadrupole splitting than those with no bridging ligands.

Support of the assignment of the components of the Mössbauer spectra of the butterfly clusters is obtained from the electric field gradient calculations. In the Mössbauer spectrum of the unprotonated mixed-metal butterfly clusters VI–VIII, the doublet with the smallest ΔE_Q is unambiguously assigned to the backbone Fe(3) atom. For each of these clusters, it is found that this iron site also has the smallest calculated value of ΔE_Q. For the protonated clusters IX and X, it is found that the backbone Fe(3) atom has the smallest calculated ΔE_Q value. This

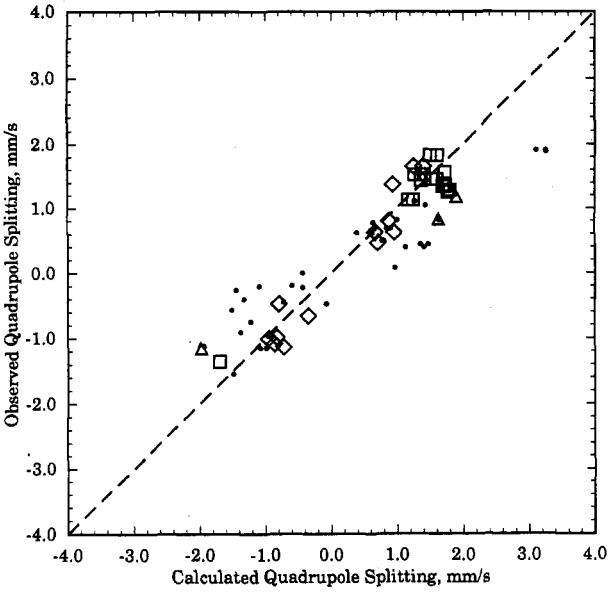

Figure 12. Observed and calculated quadrupole interactions for the unprotonated wingtip iron (□), the protonated wingtip iron (△), and the backbone iron (◇). The smaller points represent values obtained for a variety of related clusters (see text for references). The dashed line is the unit slope and *not* a fit to the data.

supports the assignment of the doublet with the smallest ΔE_Q to the backbone Fe(3) site in all of the protonated clusters.

Table V and Figure 12 reveal several doublets for which there are rather large discrepancies between the observed and the calculated values of ΔE_Q. For example, in clusters I, IX, and X this difference for the protonated wingtip iron Fe(1) site is 0.8 mm/s. One possible explanation for this disagreement is our neglect of the Sternheimer γ_∞ and R factors, which should be included in the calculated value of the electric field gradient. These factors account for the polarization of the symmetric electronic core by the nonspherical valence and lattice electronic distributions. Because the lattice contribution to the electric field gradient is very small, the γ_∞ lattice antishielding factor must be negligible. However, for the protonated wingtip iron in I, IX, and X, for which the calculated ΔE_Q value is greater than the observed ΔE_Q value, the Sternheimer shielding factor, R, will reduce the overall electric field gradient and thus the calculated value of ΔE_Q. Another possible explanation for this disagreement is that for some of the clusters the structure used for the molecular orbital and electric field gradient calculations was not the crystal structure for the compound but a symmetrized or approximated structure. We have found that differences in bond lengths of 0.02 Å will change the molecular orbital wave function coefficients and in turn the electric field gradient by up to 15%. Finally, a disagreement between the observed and calculated values of ΔE_Q could result from the use of a nonideal basis set for the metal atoms.

Conclusions

We have shown how changes in the electronic environment of these clusters may be better understood through Fenske–Hall molecular orbital calculations. The additional anionic charge is delocalized over the entire cluster; however, the majority of the additional anionic charge is localized on the carbonyl ligand oxygen atoms. The carbide and carbonyl ligand charges are influenced by the electronegativity of the iron and the heterometal and by the carbon–metal overlap populations. The charges of the Lewis base ligands become more negative as the electronegativity of the heterometal becomes smaller. In contrast, the charges of the Lewis bases become less negative as the ligand to metal overlap population decreases. A more negative carbide or carbonyl ligand charge results in less electron density localized on the metal and, hence, a decrease in the metal atomic orbital population. The charge of the backbone M(2) atom is also found to become more positive as the electronegativity of the metal becomes smaller. The replacement of the backbone Fe(2) atom with a different transition metal changed only slightly the electron environment of the remaining iron atoms. The iron charges became slightly more negative as the electronegativity of the heterometal became smaller. The iron electronic environment is found to depend more upon the carbide and carbonyl ligand near neighbors than upon the kind of near-neighbor metal atom.

This study has shown that the Mössbauer effect is very sensitive to the changes in the electronic environment of an iron site in homo- and heterometallic organoiron clusters. The Mössbauer-effect isomer shifts reveal two rather different electronic environments at the iron sites in the butterfly clusters. The isomer shifts of the backbone and protonated wingtip iron sites are more positive than those of the unprotonated wingtip iron sites. The isomer shifts were successfully related to the bonding in the clusters through the iron 4s overlap populations. It was found that a larger iron 4s to near-neighbor overlap population, which represented a larger s-electron density at the iron nucleus, corresponded to a smaller isomer shift. When the isomer shift is represented by the sum of the iron 4s population and the effective nuclear charge experienced by the iron 4s electrons, the Mössbauer-effect isomer shifts and the results of the Fenske–Hall molecular orbital calculations are consistent. It follows then that the Fenske–Hall molecular orbital calculations are indeed successful in distinguishing experimentally known differences in the iron s-electronic densities in clusters of similar structure.

The electric field gradient may be successfully calculated from the iron molecular orbital wave functions. In these clusters the major contribution to the electric field gradient is the valence contribution, the lattice contribution being at most 5%. The calculated values of ΔE_Q were found to be at most 0.8 mm/s larger or 0.5 mm/s smaller than the observed values of ΔE_Q. The values of ΔE_Q for the wingtip iron atoms are greater than those for the backbone iron atoms, indicating a more asymmetric electronic environment at the wingtip iron site.

Acknowledgment. We thank the donors of the Petroleum Research Fund, administered by the American Chemical Society, for their support of this work. We also wish to thank Drs. L. Biolsi, G. Bertrand, A. Penico, F. Grandjean, C. G. Benson, and D. E. Tharp for their helpful discussions and Drs. D. F. Shriver, J. A. Hriljac, and J. W. Kolis for the samples.

OM920753X